International Journal of Heat and Mass Transfer 52 (2009) 4851–4861

Contents lists available at ScienceDirect

International Journal of Heat and Mass Transfer

journal homepage: www.elsevier.com/locate/ijhmt

Numerical simulation of thermal convection of viscoelastic fluids using the grid-by-grid inversion method

H.M. Park *, K.S. Shin, H.S. Sohn

Department of Chemical and Biomolecular Engineering, Sogang University, Seoul, South Korea

ARTICLE INFO

Article history:
Received 6 January 2009
Received in revised form 2 May 2009
Accepted 2 May 2009

Keywords:
Differential constitutive equation
Instability
Numerical

ABSTRACT

Rayleigh–Bénard convection of viscoelastic fluids in a cavity is investigated using a newly developed grid-by-grid inversion method. In the grid-by-grid inversion method the hyperbolic constitutive equation is split such that the term for the convective transport of stress tensor is treated as a source. This renders the stress tensor a local function of the velocity gradient tensor as in the case of the Newtonian fluids and makes the algorithms for Newtonian fluids applicable to viscoelastic fluids. To corroborate the accuracy of the grid-by-grid inversion method, a linear stability analysis is performed to find the critical Rayleigh number and the domains of Hopf bifurcation and exchange of stabilities in the parameter space. The numerical results from the grid-by-grid inversion method are found to coincide with those of linear stability analysis exactly. Also considered is the standard benchmark problem of viscoelastic flow past a cylinder placed at the center between two plates to confirm the accuracy of the grid-by-grid inversion method.

1. Introduction

Numerical simulation of isothermal viscoelastic flows has been investigated extensively during last decades. However, fluid flow is strongly influenced by heat transfer in most real industrial operations. Intriguing questions associated with numerical simulation of nonisothermal viscoelastic flows are how to find appropriate type of constitutive equations describing the momentum and heat transfer in viscoelastic fluids and how to deal with storage of elastic energy in addition to difficulties inherent in the computation of isothermal viscoelastic flows [1–3].

In the present investigation, we consider the Rayleigh–Bénard convection of viscoelastic fluids in a two-dimensional cavity. The Rayleigh–Bénard convection is one of the most extensively studied problem of hydrodynamic stability due to its frequent occurrence in various fields of science and engineering. A full account of the linearized theory for Newtonian fluids is well documented in Chandrasekhar [4]. The linear stability analysis has been extended to viscoelastic fluids in a finite domain later [5]. The linear stability analysis yields the minimum Rayleigh number or the minimum temperature difference imposed on the system over which the convective flow sets in. The availability of the linear stability theory to the Rayleigh–Bénard problem makes it a good benchmark problem for a new numerical method of nonisothermal viscoelastic flows. Mathematically, a wide range of viscoelastic models are mixed type, being hyperbolic–elliptic in the steady state and hyperbolic–parabolic in the unsteady state [6]. This make the numerical simulation of viscoelastic fluids difficult since it is quite cumbersome to devise a numerical algorithm that works for mixed systems. Various numerical techniques for solving viscoelastic flows, including finite volume method, finite element method and spectral method, are well documented in the references cited [7,8]. In the present investigation, we solve the Rayleigh–Bénard convection of viscoelastic fluids in finite domains using a newly developed grid-by-grid inversion method. In the hyperbolic constitutive equations of viscoelastic fluids, the term representing the convective transport of stress tensor makes the stress field depend on the velocity gradient tensor in a nonlocal manner. If the term for convective transport of stress is assumed to be known, the constitutive equation becomes local and the stress tensor is easily evaluated for a given velocity gradient tensor at the same location. Then, the numerical solution of viscoelastic flows becomes as easy as that of Newtonian fluids. In this method, the six components of stress tensor are found in terms of the velocity gradient tensor at the same location by inverting a six-by-six matrix at each grid point. Thus, we call this algorithm the grid-by-grid inversion method. The assumed source term of the convection of stress tensor can be updated iteratively in the numerical procedure. In principle, this algorithm can be combined with finite volume method, finite element method or spectral method. In the present work, we adopt a finite volume method based on the SIMPLE algorithm [9] to implement the grid-by-grid inversion method. Regarding the constitutive equation, we adopt a general constitutive equation that encompasses the upper convected Maxwell (UCM) model, the Oldroyd B model and the PTT model with additional consideration of a realistic thermorheological behavior for the nonisothermal calculations. Wachs and Clermont [1] have used a general thermodynamic

* Corresponding author. Tel.: +82 2 705 8482.
E-mail address: hmpark@sogang.ac.kr (H.M. Park).

0017-9310/$ - see front matter © 2009 Elsevier Ltd. All rights reserved.
doi:10.1016/j.ijheatmasstransfer.2009.05.027

Nomenclature

a_T	shift parameter
C_1, C_2	parameters in WLF equation
$\mathbf{D}$	rate of deformation tensor
g	parameter defined in Eq. (7)
L	characteristic length
P	pressure
Pr	Prandtl number
Ra	Rayleigh number
Ra_c	critical Rayleigh number
t	time
$\mathbf{v}$	velocity
£	operation defined in Eq. (11)

Greek symbols

α	energy partition coefficient
α_T	thermal diffusivity
β	retardation ratio
β^t	thermal expansion coefficient
ϵ	material parameter appearing in Eq. (5)
η_0	zero-shear rate viscosity
Θ	dimensionless temperature
λ	relaxation time
μ	parameter defined in Eq. (8)
ξ	material parameter appearing Eq. (5)
$\boldsymbol{\Sigma}$	stress tensor defined in Eq. (2)
$\boldsymbol{\sigma}$	total stress tensor
$\boldsymbol{\tau}$	polymer-contributed stress tensor
ψ	stream function

Superscripts

$*$	dimensional variables
it	itth time step
n	nth iteration

framework to describe the energy conversion mechanism occurring with viscoelastic fluids and adopted the WLF equation to take into consideration the temperature dependence of the material parameters. This kind of thermodynamic consideration is essential in the investigation of nonisothermal viscoelastic flows.

To corroborate the grid-by-grid inversion method, we apply the linear stability analysis to the same system and find the critical Rayleigh number and the domains in the parameter space where the exchange of stabilities and Hopf bifurcation occur. The technique of linear stability analysis is an extension of Park and Ryu [5] and employs a Legendre spectral method [10]. To further confirm the accuracy and robustness of the grid-by-grid inversion method, we also consider a viscoelastic flow past a cylinder placed at the center between two plates, which has been served as a traditional benchmark problem.

2. Governing equations

The governing equations for nonisothermal flows of viscoelastic Boussinesq fluids are nondimensionalized by using the following dimensionless variables:

$$\mathbf{v}=\frac{\mathbf{v}^*L}{\alpha_T},\quad t=\frac{t^*\alpha_T}{L^2},\quad \boldsymbol{\sigma}=\frac{\boldsymbol{\sigma}^*L^2}{\eta_0\alpha_T},\quad P=\frac{P^*L^2}{\eta_0\alpha_T},\quad \mathbf{D}=\frac{\mathbf{D}^*L^2}{\alpha_T},$$
$$\boldsymbol{\tau}=\frac{\boldsymbol{\tau}^*L^2}{\eta_0\alpha_T},\quad \lambda=\frac{\lambda^*\alpha_T}{L^2} \tag{1}$$

Here, variables with superscript asterisk denote dimensional variables, α_T is the thermal diffusivity, η_0 is the zero-shear rate viscosity of the viscoelastic fluid, L is the depth of the cavity and λ^* is the relaxation time. Then the dimensionless governing equations may be written as:

$$\nabla\cdot\mathbf{v}=0 \tag{2}$$
$$\frac{1}{Pr}\left(\frac{\partial\mathbf{v}}{\partial t}+\mathbf{v}\cdot\nabla\mathbf{v}\right)=\nabla\cdot\boldsymbol{\sigma}+Ra\Theta\mathbf{j} \tag{3}$$
$$\boldsymbol{\sigma}=-P\mathbf{I}+2(1-\beta)a_T\mathbf{D}+\boldsymbol{\tau} \tag{4}$$
$$\lambda^0 a_T\left(\frac{\partial\boldsymbol{\tau}}{\partial t}+\mathbf{v}\cdot\nabla\boldsymbol{\tau}\right)=2\mu\beta a_T\mathbf{D}+\lambda^0 a_T(\mathbf{£}\cdot\boldsymbol{\tau}+\boldsymbol{\tau}\cdot\mathbf{£}^T)-g\boldsymbol{\tau} \tag{5}$$
$$\frac{\partial\Theta}{\partial t}+\mathbf{v}\cdot\nabla\Theta=\nabla^2\Theta+f^E\alpha\boldsymbol{\tau}:\mathbf{D}+f^E(1-\alpha)\frac{tr\boldsymbol{\tau}}{2\lambda^0 a_T} \tag{6}$$

where

$$g=1+\frac{\lambda^0\epsilon}{\beta}tr\boldsymbol{\tau} \tag{7}$$
$$\mu=\frac{1+\xi(2-\xi)(\lambda^0 a_T)^2\dot{\gamma}^2}{(1+(\lambda^0 a_T)^2\dot{\gamma}^2)^{(1-n)/2}} \tag{8}$$
$$\dot{\gamma}^2=2tr\mathbf{D}^2 \tag{9}$$
$$\mathbf{D}=\frac{1}{2}(\nabla\mathbf{v}+(\nabla\mathbf{v})^T) \tag{10}$$
$$\mathbf{£}=(\nabla\mathbf{v})^T-\xi\mathbf{D} \tag{11}$$

Here, ξ and ϵ are material parameters, λ is the dimensionless relaxation time called the Deborah number. The superscript T is the transpose, tr is the trace and β is the retardation ratio defined by $\beta=\eta_{m0}/\eta_0$, where η_{m0} is the zero-shear rate molecular-contributed viscosity. The dimensionless temperature Θ is defined by $\Theta=(T-T_t)/\Delta T$ and $\Delta T\equiv T_b-T_t$, where T_b is the temperature at the bottom of the system and T_t that at the top of the system, and $\mathbf{j}$ is the unit vector in the negative direction of the gravitational force. The dimensionless groups, Pr, Ra and f^E are defined by

$$Pr=\frac{\eta_0}{\rho\alpha_T},\quad Ra=\frac{\rho gL^3\beta^t\Delta T}{\alpha_T\eta_0}=\frac{\Delta T}{C_T},\quad C_T=\frac{\alpha_T\eta_0}{\rho gL^3\beta^t},$$
$$f^E=\frac{\alpha_T\rho gL\beta^t}{kRa} \tag{12}$$

In Eq. (12), β^t is the thermal expansion coefficient of the viscoelastic fluid defined by $\beta^t=-\frac{1}{\rho}\left(\frac{\partial\rho}{\partial T}\right)$ and α_T is the thermal diffusivity defined by $\frac{k}{\rho C_p}$. In the energy equation, the total heat source term is written in terms of the energy partitioning coefficient $\alpha;\alpha=0$ corresponds to pure energy elasticity and $\alpha=1$ corresponds to pure entropy elasticity [3]. The shift factor a_T takes care of the temperature dependence of viscosity η_0 and relaxation time λ^0 and obeys the WLF equation [12] such that

$$\ln a_T=\frac{-C_1\Theta}{(C_2/(C_T Ra))+\Theta} \tag{13}$$

In the present work, we take $C_1=4.54$ and $C_2=150.36$ K as in Wachs and Clermont [1]. For 1 cm layer of fluid, C_T is about 6.5627×10^{-5} K for most viscoelastic fluids. We solve Eqs. (2)–(13) to find the velocity and temperature fields in a two-dimensional cavity when the bottom of the cavity is hot, the top is cold and the side walls are adiabatic, i.e., $\Theta=1.0$ at $y=0.0, \Theta=0.0$ at $y=1.0$ and $\frac{\partial\Theta}{\partial x}=0$ at $x=0.0$ and 1.0. The boundary conditions for

the velocity field is nonslip. This is the traditional Rayleigh–Bénard convection problem extended to viscoelastic fluids in finite domains.

3. Numerical solution using the grid-by-grid inversion method

The convection term of the stress tensor $\boldsymbol{\tau}$ in Eq. (5), $\mathbf{v}\cdot\nabla\boldsymbol{\tau}$, makes the functional dependence of $\boldsymbol{\tau}$ on the velocity gradient tensor $\nabla\mathbf{v}$ nonlocal and necessitates boundary conditions for $\boldsymbol{\tau}$. In the grid-by-grid inversion method, $\mathbf{v}\cdot\nabla\boldsymbol{\tau}$ in Eq. (5) in assumed to be a known source term and Eq. (5) is solved for $\boldsymbol{\tau}$ in terms of local velocity gradient tensor $\nabla\mathbf{v}$. The steps for obtaining the velocity and the stress at time step $n+1$, $\mathbf{v}^{n+1}$ and $\boldsymbol{\tau}^{n+1}$, using the known velocity and stress at time step n, $\mathbf{v}^n$ and $\boldsymbol{\tau}^n$, proceed in an iterative manner as follows. First, define

$$\mathbf{C} = \mathbf{v}^{n+1(it)}\cdot\nabla\boldsymbol{\tau}^{n+1(it)} \tag{14}$$

where the superscript $n+1(it)$ indicates variables at time step $n+1$ in the itth iteration. Then Eq. (5) is discretized in the time variable as

$$\begin{aligned}\lambda^0 a_T\frac{\boldsymbol{\tau}^{n+1(it+1)}-\boldsymbol{\tau}^n}{\Delta t} = &-\lambda^0 a_T\mathbf{C}+2\mu^{n+1(it)}\frac{\beta a_T}{Re}\mathbf{D}^{n+1(it)}\\ &+\lambda^0 a_T\left(\mathbf{\pounds}^{n+1(it)}\cdot\boldsymbol{\tau}^{n+1(it+1)}+\boldsymbol{\tau}^{n+1(it+1)}\cdot\mathbf{\pounds}^{T^{n+1(it)}}\right)\\ &-g^{n+1(it)}\boldsymbol{\tau}^{n+1(it+1)}\end{aligned} \tag{15}$$

where $g^{n+1(it)}$ and $\mu^{n+1(it)}$ imply that they are evaluated by Eqs. (7) and (8) using variables at the $n+1$th time step in the itth iteration. Using Eqs. (10) and (11), $\mathbf{D}$ and $\mathbf{\pounds}$ can be replaced with the velocity gradient $\nabla\mathbf{v}$. Then, Eq. (16) becomes the following local matrix equations for $\boldsymbol{\tau}^{n+1(it+1)}$ defined at each grid point.

$$\begin{aligned}&\left(\frac{\lambda^0 a_T}{\Delta t}+g^{n+1(it)}\right)\boldsymbol{\tau}^{n+1(it+1)}\\ &-\lambda^0 a_T\left[\left(1-\frac{\xi}{2}\right)(\nabla\mathbf{v})^{T^{n+1(it)}}-\frac{\xi}{2}(\nabla\mathbf{v})^{n+1(it)}\right]\cdot\boldsymbol{\tau}^{n+1(it+1)}\\ &-\boldsymbol{\tau}^{n+1(it+1)}\cdot\lambda^0 a_T\left[\left(1-\frac{\xi}{2}\right)(\nabla\mathbf{v})^{n+1(it)}-\frac{\xi}{2}(\nabla\mathbf{v})^{T^{n+1(it)}}\right]\\ &=\frac{\lambda^0 a_T}{\Delta t}\boldsymbol{\tau}^n-\lambda^0 a_T\mathbf{C}+\mu^{n+1(it)}\frac{\beta a_T}{Re}\left[(\nabla\mathbf{v})^{n+1(it)}+(\nabla\mathbf{v})^{T^{n+1(it)}}\right]\end{aligned} \tag{16}$$

Once $\mathbf{C}$ is evaluated using variables at the previous iteration, Eq. (16) can be solved easily by inverting a six-by-six matrix at each grid point for the six independent stress components at the $n+1$ th time step in the $it+1$th iteration. Eq. (16) is also solved at the boundary grid points to find the boundary stress field. This suggests a natural method of imposing boundary conditions for the hyperbolic stress equations. After obtaining $\boldsymbol{\tau}^{n+1(it+1)}$, the velocity field at the $n+1$th time step in the $it+1$th iteration, $\mathbf{v}^{n+1(it+1)}$, is obtained by solving Eqs. (2)–(4) as follows:

$$\nabla\cdot\mathbf{v}^{n+1(it+1)} = 0 \tag{17}$$

$$\begin{aligned}&\frac{\mathbf{v}^{n+1(it+1)}-\mathbf{v}^n}{\Delta t}+\mathbf{v}^{n+1(it+1)}\cdot\nabla\mathbf{v}^{n+1(it+1)}\\ &=-\nabla P^{n+1(it+1)}+\frac{(1-\beta)}{Re}\nabla^2\mathbf{v}^{n+1(it+1)}+\nabla\cdot\boldsymbol{\tau}^{n+1(it+1)}\end{aligned} \tag{18}$$

Eqs. (17) and (18) can be solved using any numerical methods for the incompressible Navier–Stokes equation. In the present investigation, we employ a finite volume method based on the SIMPLE algorithm [9]. Eqs. (14), (16)–(18) are solved iteratively until converged velocity and stress fields are attained for the $n+1$th time step. To stabilize the numerical scheme for large values of λ^0, Eq. (14) is evaluated using any of the various upwind schemes. In the present investigation, we employ the first order upwind scheme to evaluate $\mathbf{C}$. Once the velocity field $\mathbf{v}^{n+1}$ is obtained the temperature Θ^{n+1} is found by solving Eq. (6) as follows:

$$\begin{aligned}\frac{\Theta^{n+1}-\Theta^n}{\Delta t}+\mathbf{v}^{n+1}\cdot\nabla\Theta^{n+1} = &\frac{1}{RePr}\nabla^2\Theta^{n+1}+f^E\alpha\boldsymbol{\tau}^{n+1}\\ &:\mathbf{D}^{n+1}+f^E(1-\alpha)\frac{tr\boldsymbol{\tau}^{n+1}}{2\lambda^0 a_T}\end{aligned} \tag{19}$$

We expound this algorithm for the stress equation, Eq. (16), for two-dimensional Rayleigh–Bénard convection under consideration. Denoting the components of velocity vector $\mathbf{v}$ as (v^x, v^y) and the three independent components of $\boldsymbol{\tau}$ and $\mathbf{C}$ for a two-dimensional system as $(\tau^{xx},\tau^{xy},\tau^{yy})$ and (C^{xx},C^{xy},C^{yy}), Eq. (16) can be represented by the following matrix equation, which must be solved at each grid point ij.

$$\mathbf{Ax} = \mathbf{b} \tag{20}$$

where

$$\mathbf{x} = \left(\tau_{ij}^{xx},\tau_{ij}^{xy},\tau_{ij}^{yy}\right)^{n+1(it+1)} \tag{21}$$

In the above equation, the $\mathbf{b}$ vector is composed of $\tau^{(n)}$, $\mathbf{C}^{n+1(it)}$ and $\nabla\mathbf{v}^{n+1(it)}$, while the matrix $\mathbf{A}$ is composed of the appropriate components of $\nabla\mathbf{v}^{n+1(it)}$. The specific components of $\mathbf{A}$ and $\mathbf{b}$ for the grid ij are displayed in Fig. 1.

The overall solution procedure for the grid-by-grid inversion algorithm for the Rayleigh–Bénard convection problem may be summarized as follows:

(0) $\mathbf{v}^n$ and $\boldsymbol{\tau}^n$ have been obtained in the previous time step n. The procedure for the time step $n+1$ begins as:
(1) Assume $\mathbf{v}^{n+1(it)}$ and $\boldsymbol{\tau}^{n+1(it)}$. For the first iteration, $\mathbf{v}^{n+1(it)}=\mathbf{v}^n$ and $\boldsymbol{\tau}^{n+1(it)}=\boldsymbol{\tau}^n$.
(2) Find g and μ at each grid point using Eqs. (7)–(9), respectively. Evaluate $\mathbf{C}$ in Eq. (14) using an upwind scheme.
(3) Using $\mathbf{v}^{n+1(it)}$, solve Eq. (16) for $\boldsymbol{\tau}^{n+1(it+1)}$ by inverting a three by three matrix at each grid point including the boundary grids.
(4) Solve Eqs. (17) and (18) for $\mathbf{v}^{n+1(it+1)}$ using the SIMPLE algorithm. Instead, any other Navier–Stokes solver may be employed.
(5) Convergence check for $\boldsymbol{\tau}^{(n+1)}$ and $\mathbf{v}^{(n+1)}$. If not converged, go to step (1). Otherwise, solve the energy Eq. (19) to find Θ^{n+1}.
(6) Go to step 0.

Usually convergence for the $\boldsymbol{\tau}^{(n+1)}$ and $\mathbf{v}^{(n+1)}$ coupling is attained in two or three iterations.

The case $\beta=1$ requires a slight modification to the above algorithm. In this case the viscous force term in Eqs. (3) and (4) becomes zero, rendering many algorithms for the Navier–Stokes equation inapplicable, including the SIMPLE method. The difficulty with $\beta=1$ can be circumvented by employing the EVSS formulation of Rajagopalan et al. [11]. Namely, when $\beta=1$, the total stress tensor $\boldsymbol{\sigma}$ is decomposed into pure viscous and elastic parts $-P\mathbf{I}+2a_T\mathbf{D}$ and $\boldsymbol{\Sigma}$, such that

$$\boldsymbol{\sigma} = -P\mathbf{I}+2a_T\mathbf{D}+\boldsymbol{\Sigma} \tag{22}$$

where $\boldsymbol{\Sigma}$ is defined by

$$\boldsymbol{\Sigma} = \boldsymbol{\tau}-2a_T\mathbf{D} \tag{23}$$

Substituting Eqs. (22) and (23) into Eqs. (3) and (5), we find the equations for $\mathbf{v}$ and $\boldsymbol{\Sigma}$, which can be solved following exactly the same procedure of the grid-by-grid inversion method described above.

$$
\begin{array}{c|c|c|c|c}
 & & & & n+1(it)\quad n+1(it+1) \\
\hline
\lambda^o a_T/\Delta t+ \lambda^o a_T\xi(\partial v^x/\partial x)_{ij} - \lambda^o a_T(1-\xi/2)2(\partial v^x/\partial x)_{ij} + g_{ij} & \lambda^o a_T\xi(\partial v^y/\partial x)_{ij} - \lambda^o a_T(1-\xi/2)2(\partial v^x/\partial y)_{ij} & 0 & \tau^{xx} & \lambda^o a_T/\Delta t\tau^{xx(n)}_{ij} - \lambda^o a_T C^{xx}_{ij} + 2\mu_{ij}\beta a^T (\partial v^x/\partial x)_{ij}/Re \\
\hline
\lambda^o a_T\xi/2(\partial v^x/\partial y)_{ij} - \lambda^o a_T(1-\xi/2)(\partial v^y/\partial x)_{ij} & \lambda^o a_T/\Delta t + g_{ij} & \lambda^o a_T(\partial v^y/\partial x)_{ij} - \lambda^o a_T(1-\xi/2)(\partial v^x/\partial y)_{ij} & \tau^{xy} & = \lambda^o a_T/\Delta t\,\tau^{xy(n)}_{ij} - \lambda^o a_T C^{xy}_{ij} + \mu_{ij}\beta a_T (\partial v^x/\partial y + \partial v^y/\partial x)_{ij}/Re \\
\hline
0 & \lambda^o a_T(\partial v^x/\partial y)_{ij} - \lambda^o a_T(1-\xi/2)2(\partial v^y/\partial x)_{ij} & \lambda^o a^T/\Delta t + \lambda^o a_T\xi(\partial v^y/\partial y)_{ij} - \lambda^o a_T(1-\xi/2)2(\partial v^y/\partial y)_{ij} + g_{ij} & \tau^{yy} & \lambda^o a_T/\Delta t\,\tau^{yy(n)}_{ij} - \lambda^o a_T C^{yy}_{ij} + 2\mu_{ij}\beta a_T (\partial v^y/\partial y)_{ij}/Re \\
\hline
 & ij & & ij & ij
\end{array}
$$

Fig. 1. The matrix **A** and vector **b** in Eq. (20).

4. Linear stability analysis for the Rayleigh–Bénard convection in a two-dimensional cavity

The critical Rayleigh number can be found very accurately by means of the linear stability analysis [4]. The linear stability analysis converts the governing equations to an eigenvalue problem and determine the stability of a state of the system based on the eigenvalue. If the largest real part of the eigenvalue is positive, the state is unstable and transits to another state. Otherwise, the state is stable to the noise. For the Rayleigh–Bénard convection, the eigenvalues depend on the Rayleigh number and the critical Rayleigh number is the one over which the largest real part of the eigenvalues become positive. The neutral stable state is the state for which the largest real part of eigenvalues is zero. With the linear stability analysis, if the imaginary part of the eigenvalue at the neutrally stable state is zero, the new mode or flow pattern grows monotonically without oscillation, and we say that the exchange of stabilities is valid [4]. On the contrary, if the imaginary part of the eigenvalue at the neutrally stable state is nonzero, the new mode grows with oscillation, and this instability is called overstability or Hopf bifurcation. These results from the linear stability analysis shall the exploited to corroborate the grid-by-grid inversion method soon.

The conduction state is given by:

$$\mathbf{v} = 0 \quad \text{and} \quad \Theta = 1 - y \tag{24}$$

Next, we linearize governing Eqs. (2)–(6) with respect to the conduction state for the linear stability analysis. The deviational temperature θ is defined by

$$\theta \equiv \Theta - (1 - y) \tag{25}$$

The shift factor a_T is linearized for $\theta \ll 1$ as follows:

$$\begin{aligned}
a_T &= exp\left[\frac{-c_1\Theta}{\frac{c_2}{c_T Ra}+\Theta}\right] = exp\left[\frac{-c_1(1-y)-c_1\theta}{\frac{c_2}{c_T Ra}+(1-y)+\theta}\right] \\
&= exp\left[\frac{-c_1(1-y)}{\frac{c_2}{c_T Ra}+(1-y)} + \theta\left(\frac{-c_1(1-y)}{\left(\frac{c_2}{c_T Ra}+(1-y)\right)^2} - \frac{c_1}{\frac{c_2}{c_T Ra}+(1-y)}\right)+\cdots\right] \\
&= exp\left[\frac{-c_1(1-y)}{\frac{c_2}{c_T Ra}+(1-y)}\right]\left[1 + \theta\left(\frac{-c_1(1-y)}{\left(\frac{c_2}{c_T Ra}+(1-y)\right)^2} - \frac{c_1}{\frac{c_2}{c_T Ra}+(1-y)}\right)+\cdots\right] \\
&= C^e(y) + O(\theta)
\end{aligned} \tag{26}$$

where

$$C^e(y) = exp\left[\frac{-c_1(1-y)}{\frac{c_2}{c_T Ra}+(1-y)}\right] \tag{27}$$

Furthermore,

$$\mu = 1 + O(\mathbf{v}^2) \tag{28}$$

Then the linearized set of equations is

$$\frac{1}{Pr}\frac{\partial \mathbf{v}}{\partial t} = -\nabla P' + 2(1-\beta)\nabla\cdot(C^e\mathbf{D}) + \nabla\cdot\boldsymbol{\tau} + Ra\theta\mathbf{j} \tag{29}$$

$$\frac{\partial\theta}{\partial t} = \nabla^2\theta + v^y + f^E(1-\alpha)\frac{tr\boldsymbol{\tau}}{2\lambda^o C^e} \tag{30}$$

where

$$P' = P - Ra\left(y - \frac{1}{2}y^2\right) \tag{31}$$

For a two-dimensional system, we many introduce the stream function ψ such that

$$(v^x, v^y) \equiv \left(\frac{\partial\psi}{\partial y}, -\frac{\partial\psi}{\partial x}\right) \tag{32}$$

In terms of the stream function, Eqs. (29) and (30) become

$$\begin{aligned}
\frac{\partial}{\partial t}(\nabla^2\psi) = Pr(1-\beta)\Bigg[&C^e\left(\frac{\partial^4\psi}{\partial x^4}+\frac{\partial^4\psi}{\partial y^4}\right) - \frac{\partial^2 C^e}{\partial y^2}\left(\frac{\partial^2\psi}{\partial x^2}-\frac{\partial^2\psi}{\partial y^2}\right) \\
&+2C^e\frac{\partial^4\phi}{\partial x^2\partial y^2} + 2\frac{\partial C^e}{\partial y}\frac{\partial^3\psi}{\partial x^2\partial y} + 2\frac{\partial C^e}{\partial y}\frac{\partial^3\psi}{\partial y^3}\Bigg] \\
&+Pr\frac{\partial^2}{\partial x\partial y}(\tau^{xx}-\tau^{yy}) + Pr\left(\frac{\partial^2}{\partial y^2}-\frac{\partial^2}{\partial x^2}\right)\tau^{xy} - RaPr\frac{\partial\theta}{\partial x}
\end{aligned} \tag{33}$$

$$\frac{\partial\theta}{\partial t} = \nabla^2\theta - \frac{\partial\psi}{\partial x} + f^E(1-\alpha)\frac{\tau^{xx}+\tau^{yy}}{2\lambda^o C^e} \tag{34}$$

For a two-dimensional system, the stress Eq. (5) may be linearized as;

$$\left(\lambda^o\frac{\partial}{\partial t}+1\right)\tau^{xx}=2\beta\frac{\partial^2\psi}{\partial x\partial y} \tag{35}$$

$$\left(\lambda^o\frac{\partial}{\partial t}+1\right)\tau^{yy}=-2\beta\frac{\partial^2\psi}{\partial x\partial y} \tag{36}$$

$$\left(\lambda^o\frac{\partial}{\partial t}+1\right)\tau^{xy}=\beta\left(\frac{\partial^2\psi}{\partial y^2}-\frac{\partial^2\psi}{\partial x^2}\right) \tag{37}$$

Imposing the operator $(\lambda^o\frac{\partial}{\partial t}+1)$ on Eqs. (33) and (34), τ^{xx}, τ^{xy} and τ^{yy} are eliminated in favor of ψ due to Eqs. (35)–(37).

$$\begin{aligned}&\frac{\partial}{\partial t}\left[\nabla^2\left(1+\lambda^o\frac{\partial}{\partial t}\right)\psi\right]\\&=Pr(1-\beta)\left[C^e\frac{\partial^4}{\partial x^4}\left(1+\lambda^o\frac{\partial}{\partial t}\right)\psi-\frac{\partial^2C^e}{\partial y^2}\left(\frac{\partial^2}{\partial x^2}-\frac{\partial^2}{\partial y^2}\right)\left(1+\lambda^o\frac{\partial}{\partial t}\right)\psi\right.\\&\left.+2C^e\frac{\partial^4}{\partial x^2\partial y^2}\left(1+\lambda^o\frac{\partial}{\partial t}\right)\psi+2\frac{\partial C^e}{\partial y}\frac{\partial^3}{\partial x^2\partial y}\left(1+\lambda^o\frac{\partial}{\partial t}\right)\psi+2\frac{\partial C^e}{\partial y}\frac{\partial^3}{\partial y^3}\left(1+\lambda^o\frac{\partial}{\partial t}\right)\psi\right]\\&+\frac{\partial^2}{\partial x\partial y}4\beta Pr\frac{\partial^2\psi}{\partial x\partial y}+\left(\frac{\partial^2}{\partial y^2}-\frac{\partial^2}{\partial x^2}\right)\beta Pr\left(\frac{\partial^2\psi}{\partial y^2}-\frac{\partial^2\psi}{\partial x^2}\right)\\&-RaPr\frac{\partial}{\partial x^2}\left(1+\lambda^o\frac{\partial}{\partial t}\right)\theta\end{aligned} \tag{38}$$

$$\frac{\partial}{\partial t}\left[\left(1+\lambda^o\frac{\partial}{\partial t}\right)\theta\right]=\nabla^2\left(1+\lambda^o\frac{\partial}{\partial t}\right)\theta-\frac{\partial}{\partial x}\left[(1+\lambda^o\frac{\partial}{\partial t})\psi\right] \tag{39}$$

Eqs. (38) and (39) may be rewritten as follows for the convenience of the linear stability analysis.

$$\frac{\partial\psi}{\partial t}=\Gamma \tag{40}$$

$$\begin{aligned}\nabla^2\Gamma+\lambda o\nabla^2\frac{\partial\Gamma}{\partial t}=&\frac{(1-\beta)}{Re}\left[C^e\left(\frac{\partial^4\psi}{\partial x^4}+\frac{\partial^4\psi}{\partial y^4}\right)+C^e\lambda^o\left(\frac{\partial^4\Gamma}{\partial x^4}+\frac{\partial^4\Gamma}{\partial y^4}\right)\right.\\&-\frac{\partial^2C^e}{\partial y^2}\left(\frac{\partial^2}{\partial x^2}-\frac{\partial^2}{\partial y^2}\right)\psi-\frac{\partial^2C^e}{\partial y^2}\lambda^o\left(\frac{\partial^2}{\partial x^2}-\frac{\partial^2}{\partial y^2}\right)\Gamma\\&+2C^e\frac{\partial^4\psi}{\partial x^2\partial y^2}+2C^e\lambda^o\frac{\partial^4\Gamma}{\partial x^2\partial y^2}+2\frac{\partial C^e}{\partial y}\frac{\partial^3\psi}{\partial x^2\partial y}\\&\left.+2\frac{\partial C^e}{\partial y}\lambda^o\frac{\partial^3\Gamma}{\partial x^2\partial y}+2\frac{\partial C^e}{\partial y}\frac{\partial^3\psi}{\partial y^3}+2\frac{\partial C^e}{\partial y}\lambda^o\frac{\partial^3\Gamma}{\partial y^3}\right]\\&+\frac{4\beta}{Re}\frac{\partial^4\psi}{\partial x^2\partial y^2}+\frac{\beta}{Re}\left(\frac{\partial^4\psi}{\partial y^4}-2\frac{\partial^4\psi}{\partial x^2\partial y^2}+\frac{\partial^4\psi}{\partial x^4}\right)-\frac{Gr}{Re^2}\frac{\partial\theta}{\partial x}\\&-\frac{Gr}{Re^2}\lambda^o\frac{\partial}{\partial x}\Phi\end{aligned} \tag{41}$$

$$\frac{\partial\theta}{\partial t}=\Phi \tag{42}$$

$$\Phi+\lambda^o\frac{\partial\Phi}{\partial t}=\frac{1}{RePr}\nabla^2\theta+\lambda^o\frac{1}{RePr}\nabla^2\Phi-\frac{\partial\psi}{\partial x}-\lambda^o\frac{\partial\Gamma}{\partial x} \tag{43}$$

The boundary conditions for ψ, Γ, θ and Φ are as follows:

$$\begin{aligned}&\cdot\ \text{at } y=0,1;\quad \psi=0,\quad \frac{\partial\psi}{\partial y}=0,\quad \Gamma=0,\quad \frac{\partial\Gamma}{\partial y}=0,\quad \theta=0,\quad \Phi=0.\\&\cdot\ \text{at } x=0,1;\quad \psi=0,\quad \frac{\partial\psi}{\partial x}=0,\quad \Gamma=0,\frac{\partial\Gamma}{\partial x}=0,\quad \frac{\partial\theta}{\partial x}=0,\quad \frac{\partial\Phi}{\partial x}=0.\end{aligned} \tag{44}$$

Eqs. (40)–(43) are discretized spatially using the Legendre spectral method [10]. Using the Legendre spectral method, differentiations of a function can be approximated by matrix multiplications.

$$\begin{aligned}\frac{\partial^g f}{\partial x^g}(x_i,y_j)&=\sum_{l=1}^{NX+1}\widehat{GX}^{(g)}_{i,l}f(x_l,y_j)\\\frac{\partial^g f}{\partial y^g}(x_i,y_j)&=\sum_{l=1}^{NY+1}\widehat{GX}^{(g)}_{j,l}f(x_i,y_l)\end{aligned} \tag{45}$$

where $g=1,2,4$ and $NX+1$ and $NY+1$ are the number of collocation points in the x- and y-direction, respectively. To convert Eqs. (40)–(43) to an algebraic eigenvalue problem, it is necessary to represent various spatial differentiations as matrix multiplications using Eq. (45) and remove the boundary grid values and outermost internal grid values of ψ, Γ, θ and Φ in terms of the remaining internal grid values by exploiting the boundary conditions [5]. In the following, we show how to represent the boundary grid values in terms of the internal grid values for the case of an arbitrary function ϕ with the following boundary conditions.

$$\text{at } x=\pm1;\quad \phi=0\quad\text{and}\quad\frac{\partial\phi}{\partial x}=0 \tag{46}$$

Eq. (44) in a discretized form is;

$$\begin{aligned}&\phi_{i,j}=0;\quad \phi_{NX+1,j}=0\\&\sum_{m=1}^{NX+1}\widehat{GX}^{(1)}_{lm}\phi_{m,j}=0;\quad \sum_{m=1}^{NX+1}\widehat{GX}^{(1)}_{NX+1,m}\phi_{m,j}=0\quad(1\leqslant j\leqslant NY+1)\end{aligned} \tag{47}$$

Solving Eq. (47), we can express the outermost internal grid values in terms of the remaining internal grid values:

$$\phi_{2,j}=\sum_{m=3}^{NX-1}a_m\phi_{m,j}=0;\quad \phi_{NX,j}=\sum_{m=3}^{NX-1}b_m\phi_{m,j}=0\quad(1\leqslant j\leqslant NY+1) \tag{48}$$

where

$$\begin{aligned}a_m&=\frac{\widehat{GX}^{(1)}_{1,NX}\widehat{GX}^{(1)}_{NX+1,m}-\widehat{GX}^{(1)}_{NX+1,NX}\widehat{GX}^{(1)}_{l,m}}{\widehat{GX}^{(1)}_{1,2}\widehat{GX}^{(1)}_{NX+1,NX}-\widehat{GX}^{(1)}_{1,NX}\widehat{GX}^{(1)}_{NX+1,2}}\\b_m&=\frac{\widehat{GX}^{(1)}_{NX+1,2}\widehat{GX}^{(1)}_{l,m}-\widehat{GX}^{(1)}_{1,2}\widehat{GX}^{(1)}_{NX+1,m}}{\widehat{GX}^{(1)}_{1,2}\widehat{GX}^{(1)}_{NX+1,NX}-\widehat{GX}^{(1)}_{1,NX}\widehat{GX}^{(1)}_{NX+1,2}}\end{aligned} \tag{49}$$

Then

$$\left(\frac{\partial^2\phi}{\partial x^2}\right)_{ij}=\sum_{m=3}^{NX-1}\left(\widehat{GX}^{(2)}_{i2}a^m+\widehat{GX}^{(2)}_{im}+\widehat{GX}^{(2)}_{i,NX}b_m\right)\phi_{mj} \tag{50}$$

All the other terms in Eqs. (40)–(43) are discretized in a similar manner to yield a set of differential equations in time only. We assume the following time dependence for the variables ψ, Γ, θ and Φ:

$$\psi=e^{st}\hat{\psi}_{x,y};\quad \Gamma=e^{st}\hat{\Gamma}_{x,y};\quad \theta=e^{st}\hat{\theta}_{x,y};\quad \Phi=e^{st}\hat{\Phi}_{x,y} \tag{51}$$

Then, Eqs. (40)–(43) are converted to the following matrix eigenvalue problem

$$s\boldsymbol{\beta}\cdot\mathbf{x}=\boldsymbol{\alpha}\cdot\mathbf{x} \tag{52}$$

where the eigenvector x is defined by

$$\begin{aligned}\mathbf{x}=(&\hat{\psi}_{3,3},\hat{\psi}_{4,3},\ldots,\hat{\psi}_{NX-1,NY-1};\quad \hat{\Gamma}_{3,3},\hat{\Gamma}_{4,3},\ldots,\hat{\Gamma}_{NX-1,NY-1},\theta_{2,2},\\&\theta_{3,2},\ldots,\theta_{NX,NY};\quad \Phi_{2,2},\Phi_{3,2},\ldots,\Phi_{NX,NY})^T\end{aligned} \tag{53}$$

Solving the matrix eigenvalue problem Eq. (52), we find the eigenvalues s and corresponding eigenvectors. The eigenvalues s of Eq. (52) determines the linear stability of the conduction state. The conduction state becomes unstable and convective flow sets in when the largest real part of the eigenvalues becomes positive. The critical Rayleigh number is defined as the smallest Rayleigh number when the largest real part of s is zero. When the largest real part of s is zero, the corresponding imaginary part of s may be zero or not, depending on the values of viscoelastic parameters λ^0 and β. When the imaginary part of s is zero, it is called the exchange of stabilities and the emerging convective flow grows monotonically without oscillation. On the other hand, when the imaginary part of s is nonzero, the convective flow sets in with a oscillation in

the magnitude of velocity and this state is called the overstability or Hopf bifurcation [4,13].

Fig. 2 shows the critical Rayleigh number Ra_c and the boundary separating the region of exchange of stabilities and that of Hopf bifurcation in the $\beta - \lambda^0$ plane when the aspect ratio $W/L = 2.0$, where L is the depth and W is the width of the cavity. The boundary is represented using a dashed line. As explained previously [5] the critical Rayleigh number remains the same as that of the Newtonian fluid regardless of (β, λ^0) values when the exchange of stabilities is valid. However, when the overstability occurs, the critical Rayleigh number depends on the values of (β, λ^0) and decreases as λ^0 or β increases. Fig. 3 shows the critical Rayleigh number for the aspect ratio in the range 1.0–3.0 when $\lambda^0 = 0.3, 0.6, 1.0$ or 1.3 and $\beta = 0.9$. The results show that the envelope of least eigenvalues is a piecewise smooth curve, each smooth section of the curve corresponding to a particular mode number, i.e., number of convection cells at the onset of instability. The mode number increases discretely as the aspect ratio W/L increases.

5. Numerical simulation of Rayleigh–Bénard convection of viscoelastic fluids using the grid-by-grid inversion method

In this section, we present the results of numerical simulation for the Rayleigh–Bénard convection of viscoelastic fluids using the grid-by-grid inversion method explained in Section 3 for $W/L = 2.0$. The accuracy of numerical simulation is to be corroborated using the results of hydrodynamic stability analysis, i.e., Fig. 2. The following parameter values are adopted as reference values:

$$\xi = 0.5, \quad \epsilon = 0.01, \quad \alpha_T = 1.487 \times 10^{-7}, \quad C_1 = 4.54,$$
$$C_2 = 150.36\ \text{K}, \quad C_T = 6.5627 \times 10^{-5}, \quad Pr = 7.2, \quad \alpha = 1.0 \qquad (54)$$

For the values of the Deborah number λ^0 and the retardation ratio β, we choose the sets $(\lambda^0, \beta) = (0.02, 0.1), (\lambda^0, \beta) = (0.5, 0.9)$ and $(\lambda^0, \beta) = (1.3, 0.9)$. According to Fig. 2, we find that $(\lambda^0, \beta) = (0.02, 0.1)$ is located in the domain for the exchange of stabilities while the remaining cases are located in the domain for overstability or Hopf bifurcation. The critical Rayleigh number Ra_c for

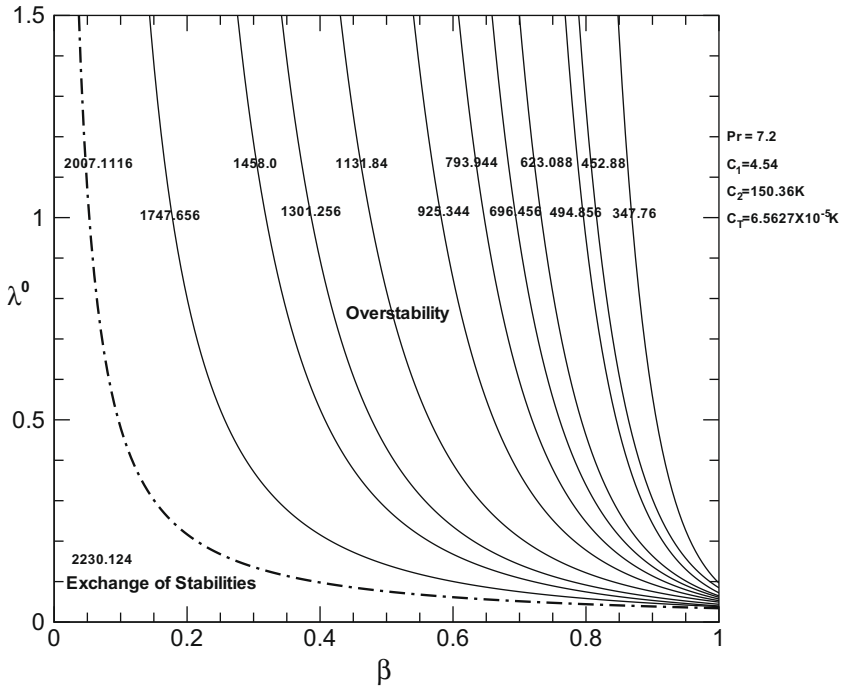

Fig. 2. The critical Rayleigh number and the boundary separating exchange of stabilities and Hopf bifurcation in the $\beta - \lambda^0$ plane for the case of $W/L = 2.0$.

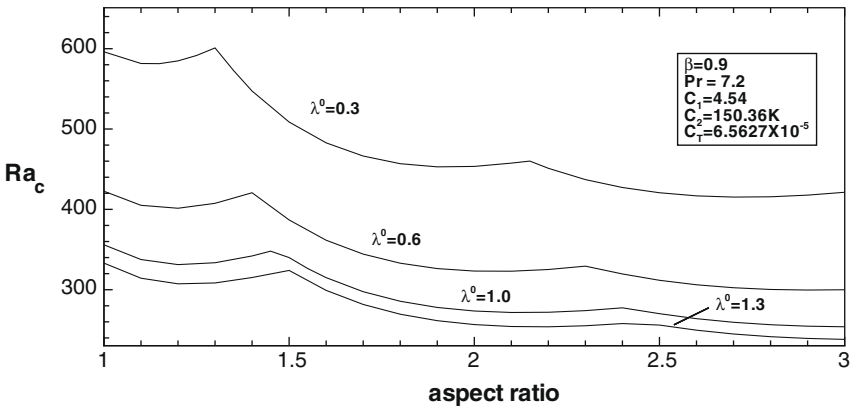

Fig. 3. Critical Rayleigh number vs. aspect ratio for various values of λ^0 when $\beta = 0.9$.

$(\lambda^0, \beta) = (0.02, 0.1)$ is 2010.135, Ra_c for $(\lambda^0, \beta) = (0.5, 0.9)$ is 348.55 and Ra_c for $(\lambda^0, \beta) = (1.3, 0.9)$ is 256.57. The number of grid points adopted for this problem is (100,100). Further increase of grid number does not change the results appreciably.

Fig. 4 shows the temporal variation of convection strength at various Rayleigh number when $(\lambda^0, \beta) = (0.02, 0.1)$. Each of Fig. 4a–e corresponds to $Ra = 0.98Ra_c, 1.01Ra_c, 17Ra_c, 18Ra_c$ and $20Ra_c$, respectively, for $Ra_c = 2010.135$. Also shown in the same figures are convection patterns at specific instants. It is shown that there is no flow when Ra is less than Ra_c (Fig. 4a). As Ra increase just over Ra_c, i.e., when $Ra = 1.01Ra_c$, convection sets in although the convection strength defined by $\int_\Omega \mathbf{v}^2 d\Omega$ is small. As anticipated from the linear stability analysis, the strength of convection is time-invariant when the Rayleigh number Ra is slightly higher than the critical Rayleigh number Ra_c for this set of rheological parameters. As Ra increases further, the steady convection is maintained with increasing strength until $Ra < 17Ra_c$. When Ra becomes $18Ra_c$, as shown in Fig. 4d, the convection strength starts to oscillate although the pattern of convection cells remain the same. When Ra increases further to $20Ra_c$, higher harmonics appear in the temporal variation of convection strength as shown in Fig. 4e. Fig. 4f is a plot of the convection strength versus Ra. For the case of overstability, the time average of convection strength is plotted. The range of exchange of stabilities is indicated

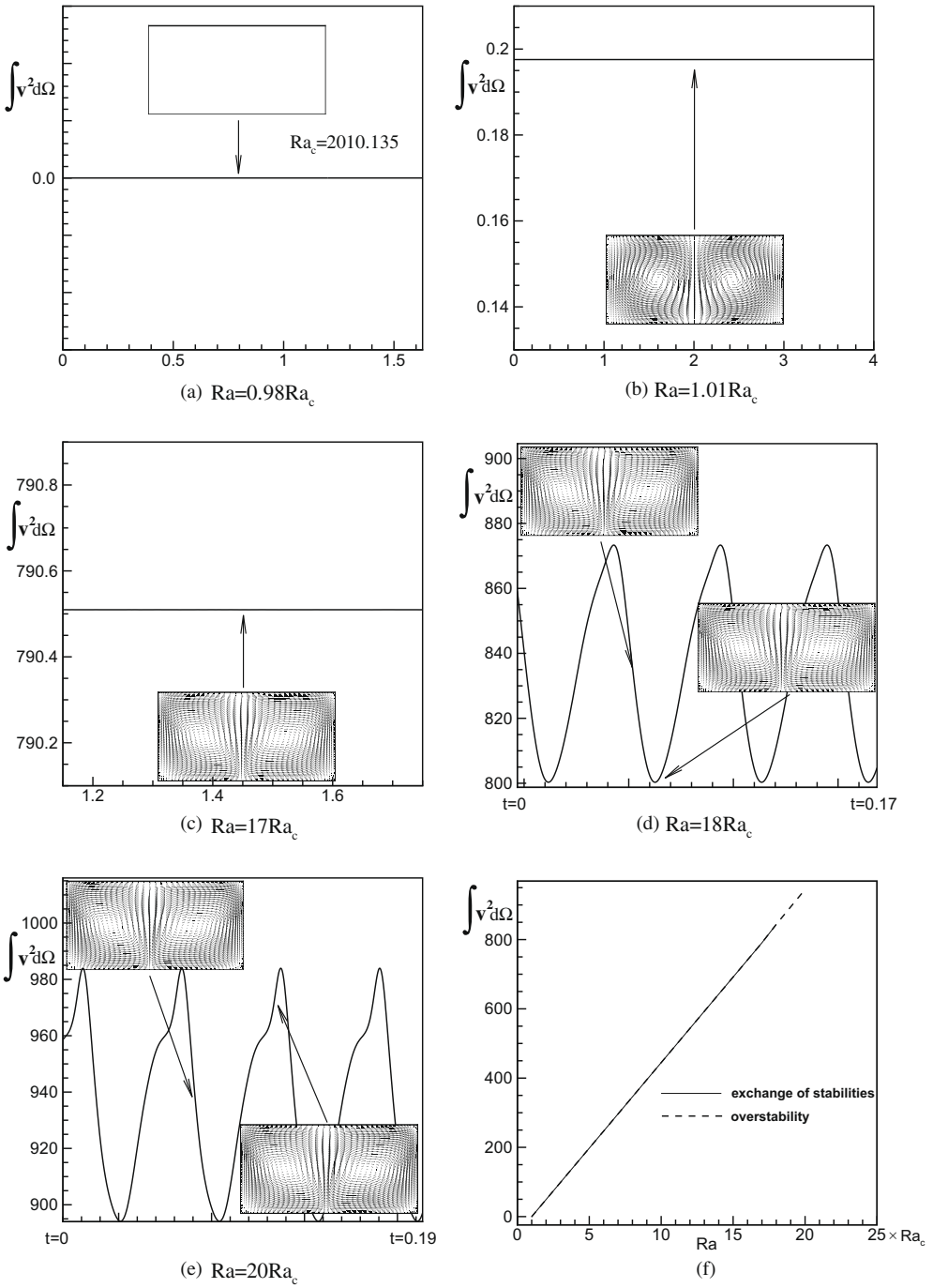

Fig. 4. Temporal variation of convection strength at various Rayleigh number when $(\lambda^0, \beta) = (0.02, 0.1)$. (a) $Ra = 0.98Ra_c$, (b) $Ra = 1.01Ra_c$, (c) $Ra = 17Ra_c$, (d) $Ra = 18Ra_c$, (e) $Ra = 20Ra_c$ and (f) convection strength versus Ra.

by a solid line and that of overstability by a dashed line. For this range of *Ra*, the convection strength varies linearly with respect to *Ra*. Fig. 5a–d shows the temporal variation of convection strength at various Rayleigh number when $(\lambda^0, \beta) = (0.5, 0.9)$. Since these values of rheological parameters are within the domain of overstability (cf. Fig. 2), the convection strength oscillates temporally at the Rayleigh number just above the critical one as shown in Fig. 5b ($Ra = 1.02Ra_c$). At $Ra = 1.02Ra_c$, the convection strength is quite weak and the convection pattern remains the same with two symmetric counter rotating cells. As *Ra* increases further to

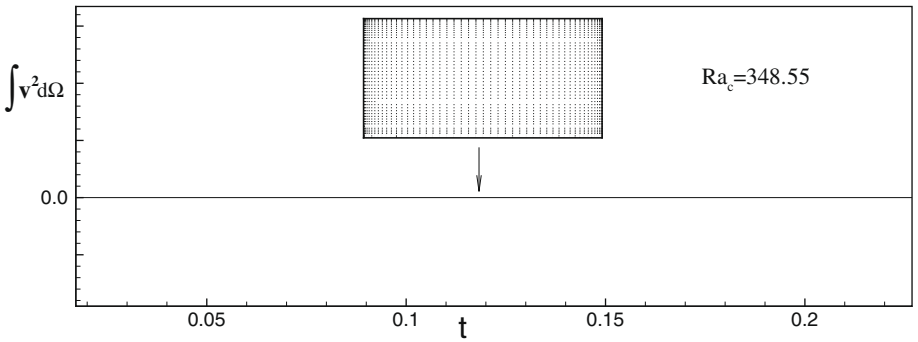

(a) $Ra=0.98Ra_c$

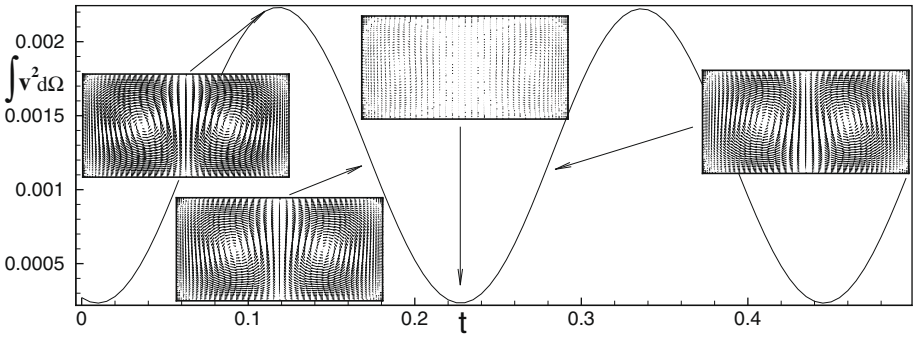

(b) $Ra=1.02Ra_c$

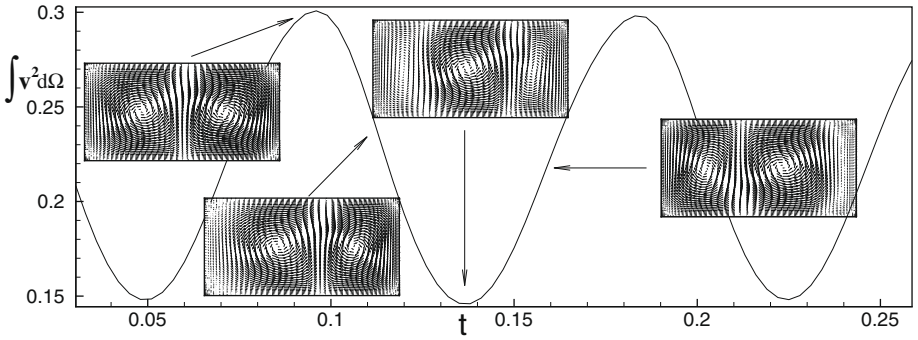

(c) $Ra=3Ra_c$

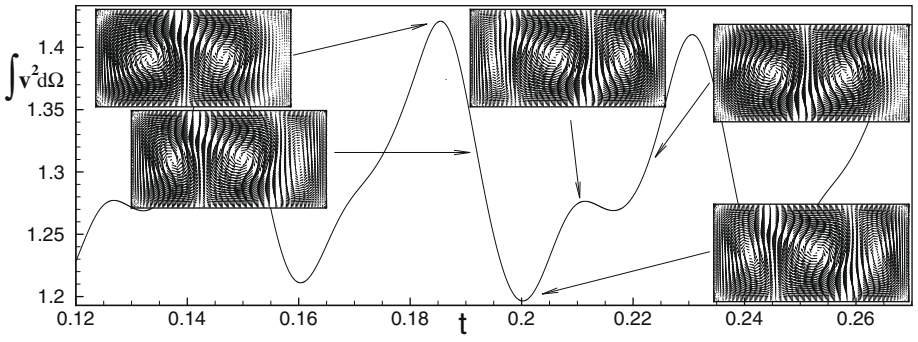

(d) $Ra=10Ra_c$

Fig. 5. Temporal variation of convection strength at various Rayleigh number when $(\lambda^0, \beta) = (0.5, 0.9)$, (a) $Ra = 0.98Ra_c$, (b) $Ra = 1.02Ra_c$, (c) $Ra = 3Ra_c$ and (d) $Ra = 10Ra_c$.

$Ra = 3Ra_c$ (Fig. 5c), the two counter rotating cells move from left to right. Further increase to $Ra = 10Ra_c$ (Fig. 5d) results in the generation of second harmonics in the temporal variation of convection strength and a third cell seems to appear in addition to the already existing two cells. Finally, we consider the case of $(\lambda^0, \beta) = (1.3, 0.9)$, which is also in the domain of overstability of Fig. 2. Obviously, these is no flow when $Ra = 0.98Ra_c$ as shown in Fig. 6a. As soon as Ra becomes larger than Ra, i.e., $Ra = 1.02Ra_c$, oscillatory convection sets in as predicted by the linear stability analysis. At $Ra = 1.02Ra_c$ (Fig. 6b), the convection pattern remains

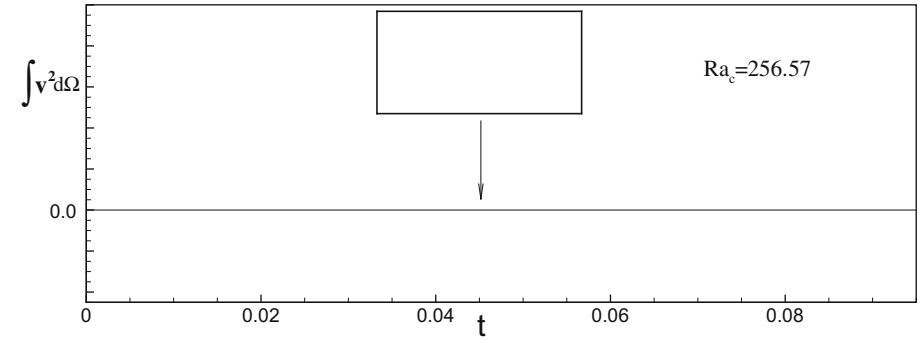

(a) $Ra=0.98Ra_c$

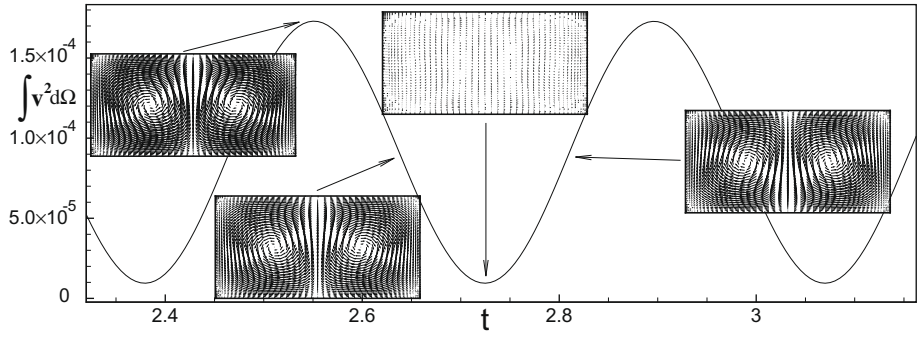

(b) $Ra=1.02Ra_c$

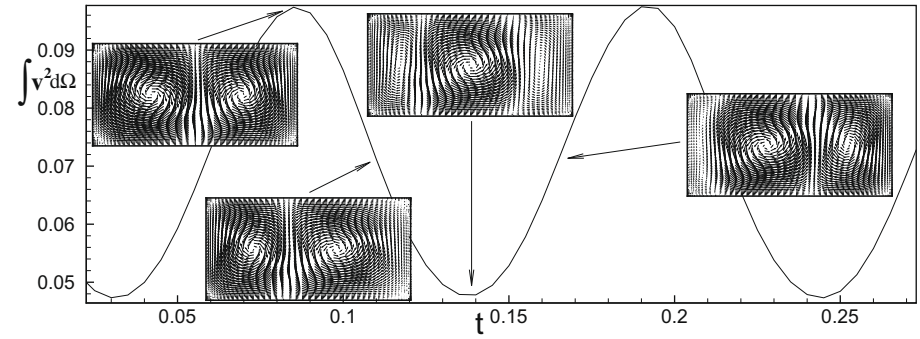

(c) $Ra=3Ra_c$

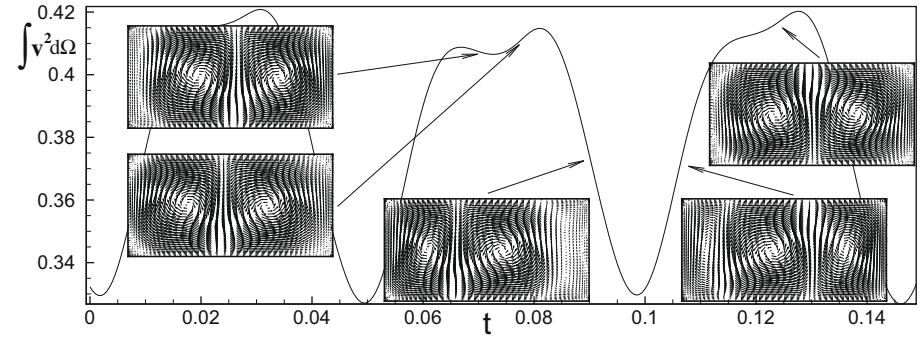

(d) $Ra=10Ra_c$

Fig. 6. Temporal variation of convection strength at various Rayleigh number when $(\lambda^0, \beta) = (1.3, 0.9)$. (a) $Ra = 0.98Ra_c$, (b) $Ra = 1.02Ra_c$, (c) $Ra = 3Ra_c$ and (d) $Ra = 10Ra_c$.

the same with two symmetric cells at a very weak convection strength. At $Ra = 3Ra_c$ (Fig. 6c), the two cells move from right to left. Increasing Ra further to $Ra = 10Ra_c$, a second harmonics appears in the temporal variation of convection strength and a third cell emerges as previously.

6. Corroboration of the grid-by-grid inversion method: viscoelastic flow past a cylinder

To corroborate the accuracy and robustness of the grid-by-grid inversion method, we solve the flow of Oldroyd B fluid past a cylinder placed at the center between two plates as depicted in Fig. 7a. This problem has been served as a traditional benchmark problem for numerical algorithms for viscoelastic fluids. Alves et al. [14] employ a finite volume method and investigate the flow of Oldroyd B model for this flow geometry. The governing equations for the isothermal Oldroyd B fluid are as follows:

$$\nabla \cdot \mathbf{v} = 0 \tag{55}$$

$$\frac{\partial \mathbf{v}}{\partial t} + \mathbf{v} \cdot \nabla \mathbf{v} = -\nabla P + \frac{(1-\beta)}{Re}\nabla^2 \mathbf{v} + \nabla \cdot \boldsymbol{\tau} \tag{56}$$

$$\lambda\left(\frac{\partial \tau}{\partial t} + \mathbf{v} \cdot \nabla \boldsymbol{\tau}\right) = \frac{2\beta}{Re}\mathbf{D} + \lambda((\nabla \mathbf{v})^T \cdot \boldsymbol{\tau} + \boldsymbol{\tau} \cdot \nabla \mathbf{v}) - \boldsymbol{\tau} \tag{57}$$

where Re is the Reynolds number. Eqs. (55)–(57) are solved for the domain of Fig. 7a using the grid-by-grid inversion method and the results are compared with those of Alves et al. [14]. To be consistent with Alves et al. [14], we set $(1-\beta) = 0.59$ and $Re = 0.0$, which is equivalent to removing the inertia force term $\mathbf{v} \cdot \nabla \mathbf{v}$ in Eq. (56). The matrix equation, Eq. (20), of the stress components for Eq. (57) becomes

$$\begin{bmatrix} 1+\frac{\lambda}{\Delta t} & -2\lambda\frac{\partial v^x}{\partial x} & -2\lambda\frac{\partial v^x}{\partial y} & 0 \\ -\lambda\frac{\partial v^y}{\partial x} & 1+\frac{\lambda}{\Delta t} & 0 & -\lambda\frac{\partial v^x}{\partial y} \\ 0 & -2\lambda\frac{\partial v^y}{\partial x} & 1+\frac{\lambda}{\Delta t} & -2\lambda\frac{\partial v^y}{\partial y} \end{bmatrix}_{ij}^{n+1(it)} \begin{bmatrix} \tau^{xx} \\ \tau^{xy} \\ \tau^{yy} \end{bmatrix}_{ij}^{n+1(it+1)}$$
$$= \begin{bmatrix} \frac{\lambda}{\Delta t}\tau^{xx(n)} - \lambda\left(v^x\frac{\partial \tau^{xx}}{\partial x} + v^y\frac{\partial \tau^{xx}}{\partial y}\right) + \frac{2\beta}{Re}\frac{\partial v^x}{\partial x} \\ \frac{\lambda}{\Delta t}\tau^{xy(n)} - \lambda\left(v^x\frac{\partial \tau^{xy}}{\partial x} + v^y\frac{\partial \tau^{xy}}{\partial y}\right) + \frac{\beta}{Re}\left(\frac{\partial v^x}{\partial y} + \frac{\partial v^y}{\partial x}\right) \\ \frac{\lambda}{\Delta t}\tau^{yy(n)} - \lambda\left(v^x\frac{\partial \tau^{yy}}{\partial x} + v^y\frac{\partial \tau^{yy}}{\partial y}\right) + \frac{2\beta}{Re}\frac{\partial v^y}{\partial y} \end{bmatrix}_{ij}^{n+1(it)} \tag{58}$$

Then we find the velocity and stress fields following the procedure of Section 3. Perhaps, the most stringent criterion for the accuracy of the numerical results for this problem comes from the stress profile in the difficult thin stress boundary layer and rear wake along the symmetry plane. A detailed comparison of the longitudinal normal stress variation along the symmetry line and cylinder surface is plotted in Fig. 7b–d at $\lambda = 0.4, 0.6$ and 0.7, respectively. Here, U is the average inlet velocity. The data of Alves et al. [14] have been obtained using 17,400 mesh points, while the number of meshes adopted for

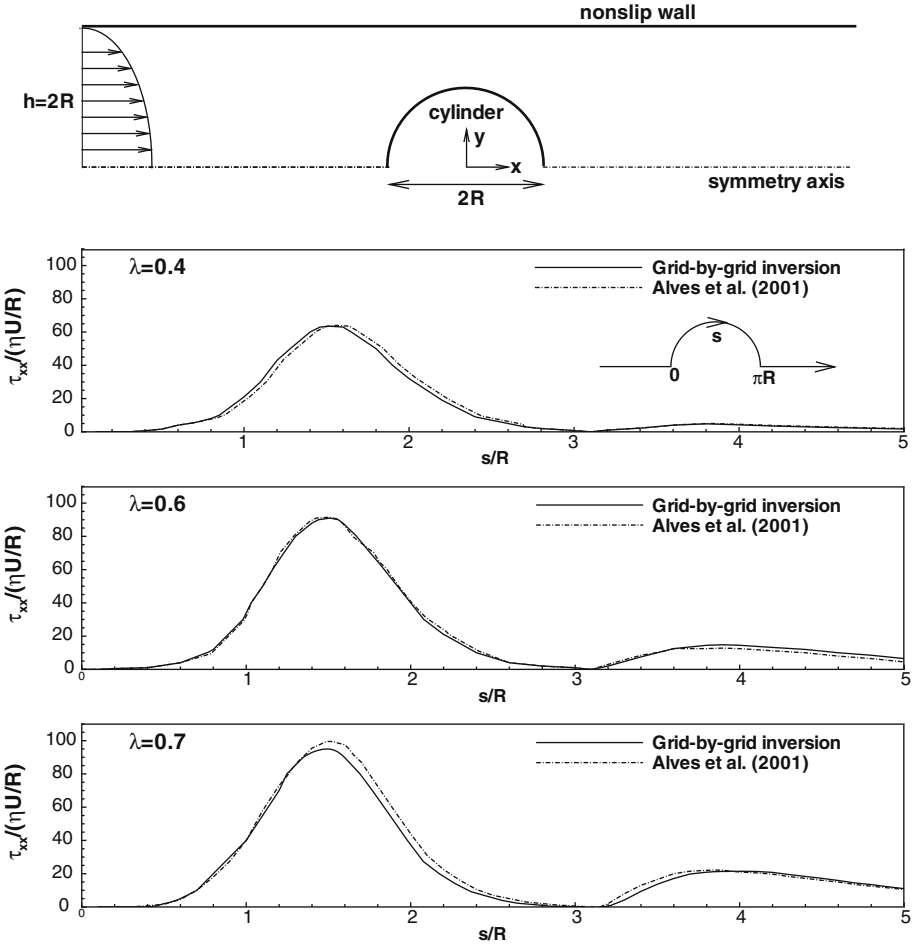

Fig. 7. Oldroyd B fluid past a cylinder. (a) flow geometry, (b) comparison of τ_{xx} along cylinder-wall and wake symmetry line for $\lambda = 0.4$, (c) the same as (b) except $\lambda = 0.6$ and (d) the same as (b) except $\lambda = 0.7$.

the grid-by-grid inversion method is 26,600. Fig. 7b–d shows that the grid-by-grid inversion method yields accurate predictions compared with the results of Alves et al. [14].

7. Conclusion

In the present investigation, we have applied the grid-by-grid inversion method to solve a nonisothermal viscoelastic flow problem. Specifically, we choose the Rayleigh–Bénard convection problem since it allows an accurate and elegant analysis of hydrodynamic stability [5,13]. The numerical results from the grid-by-grid inversion method are found to coincide with those of linear stability analysis almost exactly. The grid-by-grid inversion method solves the hyperbolic constitutive equation of viscoelastic fluid by inverting a six-by-six matrix equation for 3-D problems and a three by three matrix for 2-D problems at each grid point. The resulting viscoelastic stress is adopted as a source term in the Navier–Stokes equations. Thus, the numerical solution of viscoelastic flow problems becomes as easy as that of Newtonian fluids if the grid-by-grid inversion method is employed. Although a finite volume method is used to implement the grid-by-grid inversion method in the present investigation, one may use finite element methods or spectral methods for the implementation of the grid-by-grid inversion method without any difficulties. To corroborate the accuracy and robustness of the grid-by-grid inversion method, we have considered the standard benchmark problem of viscoelastic flow past a cylinder placed at the center between two plates. The grid-by-grid inversion method is found to yield accurate predictions compared with the results of Alves et al. [14].

References

[1] A. Wachs, J.-R. Clermont, Non-isothermal viscoelastic flow computation in an axisymmetric contraction at high Weissenberg numbers by a finite volume method, J. Non-Newtonian Fluid Mech. 95 (2000) 147–184.
[2] U.A. Al-Mubaiyedh, R. Sureshkumar, B. Khomami, Energetic effects on the stability of viscoelastic Dean flow, J. Non-Newtonian Fluid Mech. 95 (2000) 277–293.
[3] G.W.M. Peters, F.P.T. Baaijens, Modelling of non-isothermal viscoelastic flows, J. Non-Newtonian Fluid Mech. 68 (1997) 205–224.
[4] S. Chandrasekhar, Hydrodynamic and Hydromagnetic Stability, Oxford University Press, London, 1961.
[5] H.M. Park, D.H. Ryu, Rayleigh–Bénard convection of viscoelastic fluids in finite domains, J. Non-Newtonian Fluid Mech. 98 (2001) 169–184.
[6] D. Joseph, Fluids Dynamics of Viscoelastic Liquids, Springer, 1990.
[7] R.R. Huilgol, N. Phan-Thien, Fluid Mechanics of Viscoelasticity, Elsevier, Amsterdam, 1997.
[8] R.G. Owens, T.N. Phillips, Computational Rheology, Imperial College Press, 2002.
[9] S.V. Patankar, Numerical Heat Transfer and Fluid Flow, Hemisphere, New York, 1980.
[10] C. Canuto, M.Y. Hussaini, A. Quateroni, T.A. Zang, Spectral Methods in Fluid Mechanics, Springer, Berlin, 1987.
[11] D. Rajagopalan, R.C. Armstrong, R.A. Brown, Finite element methods for calculation of steady viscoelastic flow using constitutive equations using a Newtonian viscosity, J. Non-Newtonian Fluid Mech. 36 (1990) 159–192.
[12] J.D. Ferry, Viscoelastic Properties of Polymer, Wiley, New York, 1980.
[13] H.M. Park, K.S. Park, Rayleigh–Bénard convection of viscoelastic fluids in arbitrary finite domains, Int. J. Heat Mass Transfer 47 (2004) 2251–2259.
[14] M.A. Alves, F.T. Pinho, P.J. Oliveira, The flow of viscoelastic fluids past a cylinder: finite volume high-resolution methods, J. Non-Newtonian Fluid Mech. 97 (2001) 207–232.